

**CHELSA-TraCE21k ~~– v1.0. Downscaled~~High resolution (1 km)
transient temperature and precipitation data since the last glacial
maximum**

Dirk Nikolaus Karger¹, Michael P. Nobis¹, Signe Normand², Catherine H. Graham¹, Niklaus E.
Zimmermann¹

¹Swiss Federal Research Institute WSL, Zürcherstrasse 111, 8903 Birmensdorf, Switzerland

²Aarhus University, Ny Munkegade 116, 8000 Aarhus, Denmark

Correspondence to: Dirk N. Karger (dirk.karger@wsl.ch)

Abstract. High-resolution, downscaled climate model data are used in a wide variety of applications across environmental sciences. ~~Here we introduce a new, high-resolution dataset, CHELSA-TraCE21k. It is obtained by downscaling TraCE-21k data, using the CHELSA V1.2 algorithm with objective to create global monthly climatologies for temperature and precipitation at 30-arc sec spatial resolution in 100-year time steps for the last 21,000 years.~~Here we introduce the CHELSA-TraCE21k downscaling algorithm to create global monthly climatologies for temperature and precipitation at 30-arc sec spatial resolution in 100-year time steps for the last 21,000 years. Paleo orography at high spatial resolution and for each timestep is created by combining high resolution information on glacial cover from current and Last Glacial Maximum (LGM) glacier databases and interpolations using a dynamic ice sheet model data (ICE6G) and a coupling to mean annual temperatures from TraCE-21k (Transient Climate Evolution of the last 21,000 years) based on the Community Climate System Model version 3 (CCSM3). Based on the reconstructed paleo orography, mean annual temperature and precipitation was downscaled using the CHELSA (Climatologies at high resolution for the Earth's land surface areas) V1.2 algorithm. The data were validated by comparisons with the glacial extent of the Laurentide ice sheet based on expert delineations, proxy data from Greenland ice cores, historical climate data from meteorological stations, and a dynamic simulation of species distributions throughout the Holocene. ~~Validations show that CHELSA-TraCE21k V1.0 dataset reasonably represents the distribution.~~Validations show that CHELSA-TraCE21k output creates a reasonable representation of the distribution of temperature and precipitation through time at an unprecedented 1km high-spatial resolution, and simulations based on the data are capable of detecting known LGM refugia of species.

1 Introduction

Since the Last Glacial Maximum (LGM), variation in climate has caused multiple changes of the Earth surface, including the rearrangement of species distributions, or even species extinctions (Prentice et al., 1991; Velichko et al., 1997; Adams and Faure, 1997; Williams et al., 2004; Yu et al., 2010; Binney et al., 2017). Yet we have not fully evaluated the historical underpinnings of these changes as we have often lacked the climate data at the necessary spatial resolution. Biological entities

Field Code Changed

such as species usually encounter climatic conditions at spatial resolutions < 1 km (Seo et al., 2009) that is beyond the spatial resolution of numerical global circulation models (GCM's) which run at much coarser spatial resolution (e.g. > 0.5°). For many applications such as inference of ecological niches (Hutchinson, 1957), determination of growing seasons (McMaster and Wilhelm, 1997), identification of species migrations (Engler and Guisan, 2009), or modelling of high resolution species distributions (Guisan and Zimmermann, 2000; Guisan and Thuiller, 2005), temporal and spatial variability in temperature and precipitation is of utmost importance. For such analyses, imprecisions in the underlying climate data can strongly deteriorate the analytical power (Soria-Auza et al., 2010).

For the recent past, the gap between the coarse GCM resolution and the high resolution needed for many ecological applications has been bridged using statistical downscaling (Wilby et al., 1998; Wood et al., 2004; Schmidli et al., 2006; Maraun et al., 2010; Karger et al., 2017a, 2020), dynamical downscaling (Skamarock et al., 2019), or interpolation of meteorological station data (Daly et al., 1997; Hijmans et al., 2005; Meyer-Christoffer et al., 2015; Harris et al., 2020). While all of these methods work comparably well for current climatic conditions, station data are not available before the 19th Century (end of the 20th century for satellite data), hampering an application of said methods to paleo-climatic models. Most paleoclimatic data at high spatial resolution is therefore based on climatologically aided interpolation (or change factor method) of GCM output (Brown et al., 2018). This process uses the high-resolution information of current day climatologies, and adds an interpolated anomaly derived from a coarser-resolution GCM (Willmott and Robeson, 1995; Hunter and Meentemeyer, 2005). While this approach works rather well for short term time series where topography is relatively stable (Daly et al., 1997), it becomes impractical for longer time series where the dependence structure between variables (e.g. topography and climate) is dynamic (Maraun, 2013). This phenomenon is of concern especially in the last 21'000 years, as the topography in many regions on Earth has changed drastically due to the retreating ice sheets and glaciers in polar regions and in high mountain areas (Scotese, 2001). While numerical climate models are able to simulate paleo-environmental conditions comparably well (Sepulchre et al., 2020), they are however, computationally very demanding, and therefore they have not been applied on ecologically relevant spatial resolutions of ≤ 1 km yet. Current global kilometer-scale models only show a simulation throughput of 0.043 SYPD (simulated years per day) (Fuhrer et al., 2018), which is 25-fold lower than computational efficient simulations of 1 SYPD (Schulthess et al., 2018; Schär et al., 2019). Even with state-of-the-art supercomputers and climate models this gap can only be minimized by a factor of 20 (Neumann et al., 2019).

Climate impact studies however, often only use a reduced set of climate variables compared to those available from the output of numerical climate models (Frieler et al., 2017). Such studies do therefore not need a complete representation of all climate processes at high spatial resolution. In ecological studies, for instance, precipitation is often used along with minimum and maximum temperatures for analyses of species occurrences (Woodward et al., 1990). Also, it is common practice to describe species ranges by their climate envelopes, thus species distribution models (SDMs) are often built using a relatively small set of climate predictors based on monthly minimum and maximum temperature and precipitation (Guisan and Zimmermann, 2000; Guisan and Thuiller, 2005).

Field Code Changed

65 Here we present paleo-climatic data, downscaled from the CCSM3 TraCE21k (Transient climate evolution of the last 21,000 years using the Community Climate System Model Version 3) model output (hereafter: TraCE21k) to a 30-arc sec. resolution using the CHELSA V1.2 (Climatologies at high resolution for the Earth's land surface areas) algorithm (Karger et al., 2017a), which covers time steps of 100 years from 21k-BP to 1950 plus some additional 4 timesteps until 1990 (Karger et al., 2017a), which covers time steps of 100 years from 21k-BP to 1950 plus some additional 4 timesteps until 1990 (TraCE21k), for minimum and maximum temperatures, surface precipitation, and paleo-orography.

70 2 Input data

2.1 Transient climate simulations TraCE-21k

The TraCE-21k (Transient climate evolution of the last 21,000 years) simulation using the CCSM3 (Community Climate System Model Version 3) climate model (Liu et al., 2009; He, 2011; Marcott et al., 2011; Carlson et al., 2012) provides information on climate change over the last 21,000 years, i.e. from Last Glacial Maximum (LGM, hereafter defined as 21k BP 75 similar to Ehlers et al. 2011) to present. The TraCE-21k simulation reproduces many main features of post-glacial climate dynamics in various parts of the world from low to high latitudes and includes abrupt climate changes (Liu et al., 2009; He, 2011). The TraCE-21k simulation output has a T31_gx3v5 resolution (Otto-Bliesner et al., 2006). It uses a coarse resolution dynamic global vegetation model (DGVM). The coupled atmosphere-ocean model in CCSM3 is based on the Community Atmospheric Model 3 (CAM3), 80 on 26 vertical hybrid coordinate levels. The land and atmosphere components in CCSM3 in the TraCE-21k simulations uses the same resolution. The parameterizations of the DGVM are largely based on the Lund-Potsdam-Jena (LPJ)-DGVM. The ocean model in CCSM3 uses the NCAR (National Center for Atmospheric Research) version of the Parallel Ocean Program (POP) with 25 vertical levels and the sea ice model is the NCAR Community Sea Ice Model (CSIM).

2.2 Observational climatology: CHELSA V1.2

85 CHELSA (Climatologies at high resolution for the Earth's land surface areas) V1.2 is a high-resolution (30-arc sec.) climate data set for earth land surface areas (Karger et al., 2017b). It includes monthly daily 2m mean, minimum, and maximum temperature, and monthly precipitation rates at 30 -arc sec resolution for the time period 1979-2013. CHELSA V1.2. is calculated on the CHELSA V1.2 topographic downscaling algorithm (Karger et al., 2017a), using the ERA-Interim (ECMWF Re-Analysis-Interim) interim reanalysis (Berrisford et al., 2009) as forcing 90 data and GPCC (Global Precipitation Climatology Center) data (Meyer-Christoffer et al., 2015) for its bias correction.

2.2 Transient glacial extent simulations: ICE6G

We used the output data of the ICE6G_C (hereafter ICE6G) model as a basis for the extent of the major ice sheets at 1° resolution. ICE6G is a refinement of the ICE5G (VM2) model (Peltier, 2004) which has been widely used to model the

Formatted: English (United States)

Formatted: Font: Not Bold

95 distribution of major ice sheets through time. The ICE6G model explicitly outputs changes in ice thickness of
major ice sheets (e.g. the Laurentide ice sheet) from the LGM till today (Argus et al., 2014; Peltier
et al., 2015) at 500 year time steps.

2.3 Observational glacial extent at Last Glacial Maximum (LGM)

100 As extent of the glaciers during the LGM,
we use data from Ehlers et al. (2011) that presents an detailed overview of Quaternary glaciations all over the
world, not only with regards to stratigraphy but also with regards to major glacial landforms and the extent of the respective
ice sheets.

2.4 Observational current glacial extent: GLIMS

105 The GLIMS (Global Land Ice Measurements from Space) project (Raup et al., 2007) at the NSIDC (National Snow and Ice
Data Center) provides data on global glacial extent and other information about glaciers including metadata on how those
outlines were derived. Here we use this database to delineate the current extent of the glaciers at high resolution globally.

2.5 Global Multi-resolution Terrain Elevation Data 2010 (GMTED2010)

110 The Global Multi-resolution Terrain Elevation Data 2010 (GMTED2010) (Danielson and Gesch, 2011) dataset contains
elevation data for the globe collected from various sources. Here we use the 30-arc sec. version of the data that represents the
mean elevation of all 7.5-arc sec. grid cells that represent the highest available resolution of the data.

2.6 Bathymetric DEM

115 We use the General Bathymetric Chart of the Oceans (GEBCO) 2014 (Weatherall et al., 2015) as bathymetry. Although
GEBCO also includes land surface altitude, we only use it for the oceans, and we keep as land altimetric data that of the
CHELSA V1.2 [algorithm \(that being GMTED2010\)](#) to maintain comparable topography at the land surface.

2.7 Global sea-level change

120 We used data from Miller et al. (2005) for the estimation of global sea-level change from 21k BP to 1990. The data provide
global estimates of sea level change over the last 100 million years. The entire time series of sea-level change is based on a
variety of proxy data, with the data used here, dating back to the LGM, being mainly based on tropical reef proxies (Miller et
al., 2005).

Downscaling is based on the CHELSA V1.2 [algorithm](#) (Karger et al., 2017a) using forcing from TraCE-21k simulations (Liu et al., 2009; He, 2011) and involving several processing steps (Fig. 1). The CHELSA [V1.2 algorithm](#) needs a dynamic forcing in the form of GCM output (Karger et al., 2020) or gridded reanalysis data (Karger et al., 2017a, 2021b), as well as a surface orography (i.e. topography above sea level) to run a suite of downscaling algorithms for key climatic variables such as air temperature and precipitation. As the orography at different time steps between 21k BP and current times is not available [at the high resolution required for the CHELSA V1.2 algorithm](#), we approximated it using a combination of data from the digital elevation model GMTED2010 (Danielson and Gesch, 2011), large scale ice sheet configurations from ICE6G (Peltier et al., 2015), high resolution glacier extents from GLIMS for current conditions (Raup et al., 2007) and LGM conditions (Ehlers et al., 2011), as well as sea level change data from Miller et al. (2005) (Fig. 1). We then ran the CHELSA [V1.2 algorithm](#) on the paleo-orography using a bias corrected version of the TraCE-21k simulations as forcing. Details on these steps are described in the following sub sections.

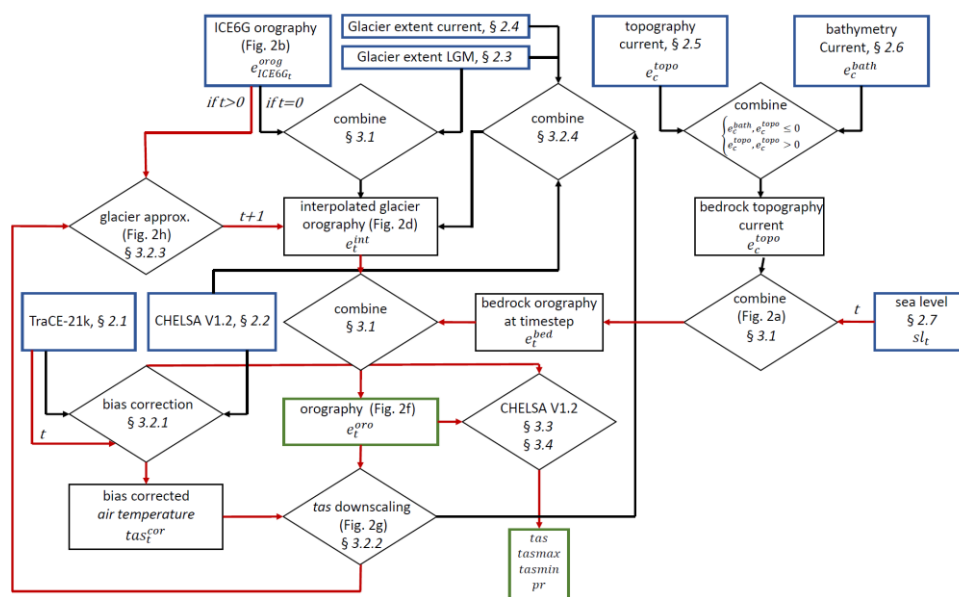


Figure 1. Graphical representation of the different steps employed in downscaling TraCE-21k simulations using the CHELSA V1.2 algorithm. Input datasets are indicated by blue box, output data are indicated by a green box. Rhombi indicate

processing steps. t indicates discrete timesteps, with $t=0$ being the LGM. Red lines indicate processing steps that are run iteratively over all time steps, black lines indicate computations that were run only once.

3.1 Paleo-orography

140 The first step in estimating the paleo-orography was carried out for the LGM (21k BP). For this time point, both estimates of glacial extents from Ehlers et al., 2011 and estimates of glacier thickness from ICE6G exist. We first combined the topographic information from GMTED2010 on land, and that of GEBCO into a bedrock topography that provides the current bedrock topography e_c^{topo} (including current day glaciers, see ff.). To create a bedrock orography e_t^{bed} (i.e. topography adjusted for sea level without glaciers except for currently glaciated areas), we used the information on past sea-level changes and set all elevations to 0 so that:

145

$$e_t^{bed} = e_c^{topo} - sl_t \quad (1)$$

To include the orography of the glaciers we first converted the polygons of the glacial extents from Ehlers et al. 2011 into point locations (Fig. 2a, black dots), and extracted their elevation from e_t^{bed} (Fig. 2a) at time $t=0$ (LGM, 21k BP) resulting in the surface elevation of the glacial boundaries (gb) e_{gbt}^{bed} . To combine the high-resolution estimates from Ehlers et al. (2011), with the coarser (1°) resolution of ICE6G, we randomly sampled 100 point locations per 1° grid cell from ICE6G and again extracted the surface elevation of the glaciers from e_t^{bed} at the ICE6G timestep that is nearest to the timestep $t=0$ (LGM, 21k BP) resulting in e_{Gt} (Fig. 2b). All points that did not fall within the high-resolution glacial extent were omitted so that only point within the high-resolution estimate of glacial extent from Ehlers et al. (2011) remained (Fig. 2b). Then both point datasets e_{gbt}^{bed} and e_{ICE6Gt}^{orog} were combined to represent a point sample of the surface elevation e_{Gt} within the high-resolution glacial extent of Ehlers et al. (2011) (Fig. 2c). Next, this point sample was spatially interpolated to a grid of 30-arc sec. resolution applying multilevel B-spline interpolations. By this, we achieved an interpolated gap free high-resolution estimate of glacial surface elevation e_t^{int} at $t=0$ (LGM, 21k BP) (Fig. 2d). The multilevel B-splines use a B-spline approximation to e_{Gt} and start using the coarsest grid ϕ_0 from an overall set of grids $\phi_0, \phi_1, \dots, \phi_n$ with $n = 14$ generated using optimized B-spline refinements (Lee et al., 1997). The resulting B-spline function $f_0(e_{Gt})$ then gives the first approximation of $e_t^{int} = f_0(e_{Gt})$ and leaves a deviation:

155

160

$$\Delta^1 e_t^{int} = e_t^{int} - f_0(x_c, y_c) \quad (2)$$

165 at each grid cell c location (x_c, y_c, e_t^{int}) . Then the next control lattice ϕ_1 is used to approximate $f_1(\Delta^1 e_t^{int}_c)$. This approximation is then repeated on the sum of:

$$f_0 + f_1 = e_t^{int} - f_0(x_c, y_c) - f_1(x_c, y_c) \quad (3)$$

at each grid cell c (x_c, y_c, e_c^{int}) n times resulting, in our case, in the gap free interpolated glacial surface e_t^{int} . The interpolated glacial surface was then combined with e_t^{bed} to the topography e_t (Fig. 2e) using:

$$e_t = \begin{cases} e_t^{topo}, & e_t^{topo} \geq e_t^{int} \\ e_t^{int}, & \text{otherwise} \end{cases} \quad (4)$$

The final orography e_t^{oro} at timestep $t=0$ (i.e. topography above sea level) (Fig. 2f) is then generated using:

$$e_t^{oro} = \begin{cases} 0, & e_t \leq sl_t \\ e_t, & e_t > sl_t \end{cases} \quad (5)$$

With sl_t being the sea-level at timestep t . Although this approach includes changes in the glacial surface and sea-level rise, it ignores changes in bedrock elevation due to upwelling after glacier melt.

3.2 Interpolation of glacier extent and thickness between LGM and current

As high-resolution estimates of glacial surface elevation are not available for timesteps t other than the LGM and current, we use a combination of mean annual 2m air temperature data, together with sea surface elevation sl_t and ICE6G orography $e_{ICE6G_t}^{oro}$ data to estimate e_t^{oro} at each time step $t \neq 0$ and $t = 221$. The rationale behind this approach is that temperature and glacier extents are interdependent, and a change in temperature will translate into a change in glacial extent or thickness. The procedure to generate high resolution glacial surfaces is explained in the following sections.

3.2.1. Bias correction of air temperature

In a first step, the orography e_t^{oro} with $t=0$ (LGM, 21k BP) was used to downscale mean annual temperature tas_t . GCMs such as the CCSM3 normally exhibit a large bias in temperatures or precipitation (Cannon et al., 2015; Maraun, 2013). We therefore applied a change factor bias correction based on the bias observed between current annual mean 2m air temperatures tas_{cur}^{obs} from CHELSA V1.2 normals resampled to a 0.5° grid resolution, and that of TraCE21k simulated for the same time period tas_{cur}^{mod} spline interpolated using same multilevel B-spline interpolation method as described in 3.1 to the 0.5° grid resolution. The resolution of 0.5° follows the same procedure as used in the CHELSA V1.2 algorithm (Karger et al. 2017). We used the time period 1980-1990 ($=cur$) to calculate this bias, as it is the only time period for which CHELSA V1.2 data and TraCE21k overlap. The change factor was then calculated as:

$$\Delta tas = tas_{cur}^{obs} - tas_{cur}^{mod} \quad (6)$$

This effectively preserves the trends observed in temperature, but simultaneously assumes that the bias has also been conserved over time (Maraun, 2016). The bias corrected temperatures tas_t^{cor} are then given by:

$$tas_t^{cor} = tas_{cur}^{obs} - \Delta tas \quad (7)$$

3.2.2. Downscaling mean annual air temperature

To achieve a high-resolution approximation of near surface air temperatures (Fig. 2g), we used a lapse rate-based downscaling from atmospheric temperature data at the TraCE-21k pressure levels. The lapse rates Γ are based on a linear approximation from average temperatures ta_z at altitudes a_z at vertical levels 26 (992.5 hPa) to 20 (600.5 hPa) of the T31_gx3v5 grid that contain all surface elevations so that:

$$\Gamma = \frac{n(\sum a_z ta_z) - (\sum a_z)(\sum ta_z)}{n(\sum a_z^2) - (\sum a_z)^2} \quad (8)$$

Temperature at the surface at a high spatial resolution tas was then calculated by:

$$tas_t = \Gamma_t * e_t^{oro} + tas_t^{cor} \quad (9)$$

3.2.3. Glacier extent approximation using mean annual air temperature

We assume that air temperature is correlated to glacier extent and use this relationship to estimate the boundaries of glaciers for each time step separately. To do so, we use mean annual 2m air temperature at the boundary of the interpolated high-resolution glacier orography. We then transformed the glacier elevations e_t^{int} , to a polygon G_t , and then transformed the outline of this polygon to a point sampling of the glacier boundaries at time $t=0$. Mean annual 2m air temperatures at this glacier boundary were then extracted for this point sample which gives the local annual mean air temperature $tas_{t=0}^{gb}$ under which a glacier had a boundary at the LGM. To set this in relation to current mean annual air temperatures at current glacier boundaries $tas_{t=221}^{gb}$ (with $t=221$ being the year 1990), we calculated the difference between current and LGM boundary temperatures. The resulting point locations for both $tas_{t=0}^{gb}$ and $tas_{t=221}^{gb}$ were then spatially interpolated using a multilevel-B-spline (as described in 3.1) to result in a gap-free surface and then subtracted resulting in Δtas_{cur}^{obs} (Fig. 2g).

As the orography for the next time step is not known yet, we estimated the near surface air temperature tas_{t+1}^{est} for the reduction in glacier extent similar the time step before. So that,

$$tas_{t+1}^{est} = \Gamma_{t+1} * e_t^{oro} + tas_{t+1}^{cor} \quad (10)$$

The binary glacial extent G_{t+1} at $t + 1$ is then approximated as:

$$G_{t+1} = \begin{cases} 1, & \text{if } \text{tas}_{t+1}^{\text{est}} < \text{tas}_t^{\text{GB}} + \frac{\Delta \text{tas}_{\text{cur}}^{\text{obs}}}{-1 + (\sum_{t-t})} \wedge G_0 = 1 \\ 0, & \text{otherwise} \end{cases} \quad (11)$$

This glacial extent is then used again to estimate the combined topography at $t+1$ in the same way as described in 3.1. As ICE6G has a 500 year resolution we used the ICE6G orography used that is closest to each timestep. As ICE6G only includes information on the major ice sheets, smaller ice sheets in the Alps do not include a sample of $e_{\text{ICE6G}_t}^{\text{orog}}$. In the case of smaller ice sheets, the surface orography from ICE6G is replaced by a point sample of the elevation of the glacier boundary under current conditions $e_{\text{gb}_c}^{\text{orog}}$ (Fig. 2h). The glacier orography in this case is then created by using a spline interpolation between $e_{\text{gb}_t}^{\text{bed}}$ and $e_{\text{gb}_c}^{\text{orog}}$. In Eq. 11 the second term in the condition for G_{t+1} linearly scales $\Delta \text{tas}_{\text{cur}}^{\text{obs}}$ over the entire number of time steps. This correction is necessary, as otherwise the entire bias would be added at the first-time step, resulting in an unrealistically strong shift in the glacial extent. We then repeated the transformation of the glacial extent G_{t+1} to all point locations and repeated the procedure for the temperature coupling to estimate the orography e_{t+1}^{oro} . Near surface air temperatures for $t + 1$ have been then approximated using,

$$\text{tas}_{t+1} = I_{t+1} * e_{t+1}^{\text{oro}} + \text{tas}_{t+1}^{\text{cor}} \quad (12)$$

3.3 Downscaling mean monthly precipitation rates

3.3.1 Orographic wind effects

The estimation of high-resolution precipitation follows a variant of the CHELSA V1.2 algorithm (Karger et al. 2017). The CHELSA V1.2 algorithm assumes that orography is one of the main drivers of precipitation (Spreen, 1947; Basist et al., 1994; Daly et al., 1997; Sevruk, 1997; Böhner, 2006; Gao et al., 2006; Böhner and Antonic, 2009; Karger et al., 2017a). In tropical convective regimes, precipitation typically increase up to the condensation level around 1000-1500 m above surface, while the exponentially decreasing moisture content in the mid- to upper troposphere results in a drying above the condensation level and in non-linear precipitation lapse rates (Körner, 2007). Furthermore, negative precipitation lapse rates are common under the extremely dry polar climates. In contrast, at mid-latitudes and in the subtropics, precipitation generally increases with increasing elevation due to advection. As a consequence, summits of the Alps or other high mountain ranges exhibit high rainfall (Rotunno and Houze, 2007), and lapse rates for precipitation are almost linear (Weischet and Endlicher, 2008). To approximate the effects of orographic precipitation we used the CHELSA V1.2 algorithm, which is explained in more detail below.

We used 10 m u -wind and v -wind components of TraCE-21k to calculate wind direction. Both wind components were projected to a world Mercator projection at a 4 km grid resolution using a multilevel B-spline interpolation similar to the one described in 3.1. Windward and leeward effects are assumed to be best represented at resolutions larger than 1 km (Daly *et al.*, 1994), we therefore chose a grid resolution of 4 km for the underlying digital elevation model. The wind effect H was then calculated using,

$$H_W = \frac{\sum_{i=1}^n \frac{1}{d_{WHi}} \tan^{-1} \left(\frac{d_{WZi}}{d_{WHi}^{0.5}} \right)}{\sum_{i=1}^n \frac{1}{d_{LHi}}} + \frac{\sum_{i=1}^n \frac{1}{d_{LHi}} \tan^{-1} \left(\frac{d_{LZi}}{d_{LHi}^{0.5}} \right)}{\sum_{i=1}^n \frac{1}{d_{LHi}}} \quad (13)$$

$$H_L = \frac{\sum_{i=1}^n \frac{1}{\ln(d_{WHi})} \tan^{-1} \left(\frac{d_{WZi}}{d_{WHi}^{0.5}} \right)}{\sum_{i=1}^n \frac{1}{\ln(d_{LHi})}} \quad (14)$$

where d_{WHi} and d_{LHi} refer to the horizontal distances between the focal 4 km grid cell in windward and leeward direction and d_{WZi} and d_{LZi} are the corresponding vertical distances compared with the focal 4 km cell following the wind trajectory. The second summand in the equation for H_W where $d_{LHi} < 0$ accounts for the leeward impact of previously traversed mountain chains. The horizontal distances in the equation for H_L where $d_{LHi} \geq 0$ lead to a longer-distance impact of leeward rain shadow. The final wind-effect parameter is calculated as $H = H_L H_W$. Both equations were applied to each grid cell at the 30-arc sec. resolution in a World Mercator projection. Orographic precipitation effects are less pronounced just above the surface, as well as in the free atmosphere above the planetary boundary layer (Daly *et al.*, 1997; Oke, 2002; Stull, 2012; Karger *et al.*, 2020). The highest impact of orography is considered just at the boundary layer height where the airflow interacts with the terrain. We used the lifted condensation level (LCL) as indicator of the altitude at which the wind effect exerts the highest contribution to precipitation. The LCL has been calculated using the mean air temperature (tas) and mean near surface relative humidity ($hurs$) using,

$$LCL = 20 + (tas/5) * (100 - hurs) \quad (15)$$

(Lawrence, 2005). The LCL has been interpolated to a 30 arc-sec. resolution using a B-spline interpolation. To create a boundary layer height corrected wind effect H_B . The wind effect grid H containing LCL was then proportionally distributed to all grid cells falling within a respective T31 grid cell using,

$$H_B = \frac{H}{1 - \left(\frac{|z - LCL_z| - z_{max}}{h} \right)} \quad (16)$$

295 With z_{max} being the maximum distance between the lifted condensation level LCL at elevation z and all grid cells at a 30-arc
 sec. resolution falling within a respective T31 grid cell, h being a constant of 9000 m, and z being the respective elevation
 from GMTED2010 (Danielson and Gesch, 2011) with,

$$LCL_z = LCL + z_{GCM} + f \quad (17)$$

300

z_{GCM} being the elevation of the TraCE21k grid cell, and f being a constant of 500 m which takes into account that the level of
 highest precipitation is not necessarily at the lower bound of the LCL, but slightly higher (Karger et al., 2017a).

The wind effect algorithm cannot distinguish extremely isolated valleys inside highly-elevated mountain areas (Frei and Schär,
 1998). Such valleys are situated in areas where the wet air masses flow over an orographic barrier and are prevented from
 305 flowing into deep valleys. These effects are mainly confined to large mountain ranges, and are not as prominent in small- to
 intermediate-sized mountain ranges (Liu et al., 2012). To account for these effects, we used a variant of the windward-leeward
 equations with a linear search distance of 300 km in steps of 5° from 0° to 355° circular for each grid cell. The calculated
 leeward index was then scaled towards higher elevations using,

$$310 \quad E = \left(\frac{\sum_{i=1}^n \frac{1}{d_{WHi}} \tan^{-1} \left(\frac{d_{LZi}}{d_{WHi}} \right)}{\sum_{i=1}^n \frac{1}{d_{LHi}}} \right) \bar{h} \quad (18)$$

c was set to 9000 m. h has been set to 9000 m. $E * H_B$ will give the first approximation of the orographic precipitation intensity
 p_I .

315 3.3.2. Bias correcting precipitation and downscaling

Precipitation, similar to temperature exhibits a rather large bias in TraCE-21k (Fig. 3, Fig. 4). To remove this bias, we applied
 a change factor bias correction similar to the one described in 3.2.1 [with the reference period 1980-1990](#). Here, we used a
 multiplicative change factor, to avoid precipitation rates < 0. Additionally, we included a constant of $c = 0.0001 \text{ kg} \cdot \text{m}^{-2} \cdot \text{month}^{-1}$,
 to avoid division by zero so that:

320

$$\Delta pr_m = (pr_{cur_m}^{mod} + c) / (pr_{cur_m}^{obs} + c) \quad (19)$$

with m being the respective month of the year. The bias corrected precipitation rate for p_m^{cor} is then calculated by:

325

$$pr_m^{cor} = pr_{cur_m}^{obs} / \Delta pr_m \quad (20)$$

To achieve the distribution of monthly precipitation pr_o given the approximated orographic precipitation intensity p_{I_c} at each grid location (x_c, y_c) , we used a linear relationship between pr_m^{cor} and p_{I_c} using,

$$pr_o = \frac{p_{I_c}}{\frac{1}{n} \sum_{i=1}^n p_{I_{ci}}} * pr_m^{cor} \quad (21)$$

where n equals the number of 30-arc sec. grid cell of p_I that fall within a 0.5 grid cell of p_m^{cor} .

3.4. Downscaling mean monthly near surface air temperatures

The downscaling of monthly near surface air temperatures (tas , $tasmax$, $tasmin$) follows the methods described in 3.2.2., with the only difference that instead of mean annual temperature, $tasmax$ and $tasmin$ are used, where $tas = (tasmax + tasmin) / 2$. The temperatures have again first been bias corrected using:

$$\Delta tasmax_m = tasmax_{cur_m}^{obs} - tasmax_{cur_m}^{mod} \quad (22)$$

$$\Delta tasmin_m = tasmin_{cur_m}^{obs} - tasmin_{cur_m}^{mod} \quad (23)$$

and:

$$tasmax_{m_t}^{cor} = tasmax_{cur_m}^{obs} - \Delta tasmax_m \quad (24)$$

$$tasmin_{m_t}^{cor} = tasmin_{cur_m}^{obs} - \Delta tasmin_m \quad (25)$$

with m being the respective month of the year, in Eq. 22 - Eq. 25.

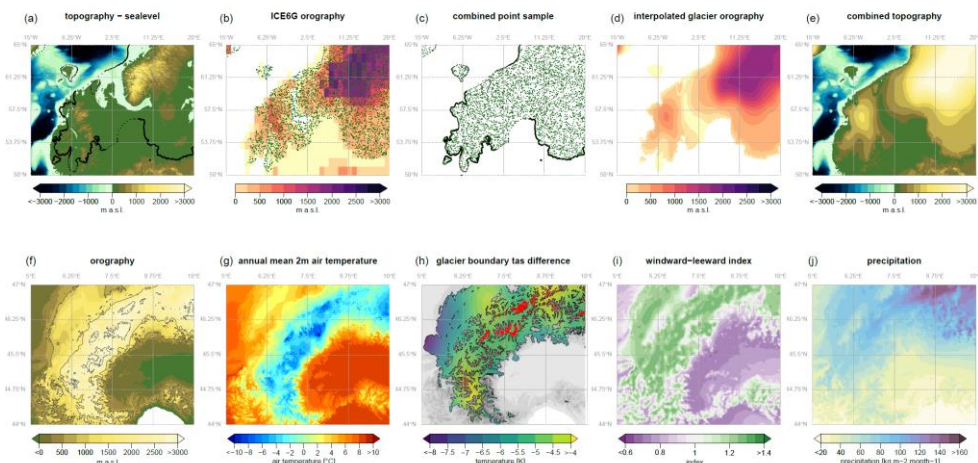


Figure 2. Illustration of several steps performed to estimate the surface orography and the temperature and precipitation fields in CHELSA-TraCE21k during the last glacial maximum (21k BP). The upper row gives an example of the interpolation of the European ice sheets, the lower row shows an example of the resulting orography and environmental variables in the western part of the European Alps. **a)** Topographic information at $t=0$ (LGM) is combined with information on past sea-levels and the boundary of ice sheets (black dots) for which the surface elevation is extracted. **b)** Within the extent of ice sheets, surface elevation is extracted from the ICE6G orography for a random sample of points for $t=0$. **c)** Both point samples from **a)** and **b)** are combined and interpolated **d)** to estimate the orography of the glaciers. **e)** The interpolated glacier orography and the sea-level adjusted topography **a)** are then combined. **f)** The high resolution (30 -arc sec) orography (shown here for the western Alps) is then used as basis at $t=0$ for **g)** a lapse-rate based downscaling of air temperature. **h)** From the high-resolution temperatures information on the glacier boundaries during the LGM (black) and current times (red) is extracted and the difference is interpolated to correct the temperature based shrinking and expansion of the glaciers. **i)** based on the orography the windward-leeward index is calculated (shown for July 21k BP), that builds the basis for the **j)** precipitation approximation.

4 Output validation

Direct validation of the temperature (Fig. 1) and precipitation (Fig. 2) output at high resolution for paleo time series generally relies on proxies, as direct observations of both variables are not available. Although global temperature time series exist, they only give global means, and do not allow validation of the performance of a 1-km paleo climatic dataset. Therefore, to validate the CHELSA-TraCE21k dataset we complement a simple comparison of the simulated time series to proxy data and current observations, with approaches of validating derived parameters from the simulated temperature and precipitation that directly benefit from a very high horizontal resolution.

4.1 Validation using current (historical) observations

We used data from the Global Historical Climate Network (GHCN) monthly database V.3 (Lawrimore et al., 2011) to validate the performance of the downscaling algorithm during the last time step of the CHELSA-TraCE21k for which station data is available. To do so we calculated monthly climatologies for each month for *tasmax*, *tasmin*, and *pr* from both TraCE-21k and CHELSA-TraCE21k. We then compared the values measured at each station to that simulated in both, TraCE-21k and CHELSA-TraCE21k.

The original TraCE-21k data shows large deviations and root mean squared errors (RMSE) from the observed data (Fig. 3). This is somewhat expected as a climate model running for such long time periods needs to have coarse resolution, as well as a large degree of generality and realism which decreases the accuracy of a model when compared to observations. The temperature variables perform well in TraCE-21k with $r \sim 0.8$ for all months, but have deviations and RMSE similar to those of precipitation, that most likely can be attributed to the coarse resolution of the climate model. TraCE-21k also seems to overestimate temperature extremes both for *tasmax* and *tasmin* (Fig. 4).

The precipitation however, does not perform well in the model with $r \sim 0.4$ and large deviations from actual values (Fig. 3) and overall precipitation seems to be too low in the model (Fig. 4).

The CHELSA [V1.2](#) algorithm improves the correlation between observed and modelled data and decreases the standard deviation for all three parameters (Fig. 3). The downscaling for the temperature variables increases the correlation to $r \sim 0.95$ for all months and decreases the standard deviation substantially (Fig. 3). Similarly, the performance of the precipitation estimation in CHELSA-TraCE21k increases, which is reflected in a $r \sim 0.7$ and a lower standard deviation and RMSE (Fig. 3). The underestimation of precipitation in the TraCE21k is reduced, but the downscaling algorithm still has a considerable bias (Fig. 3) during the historical period.

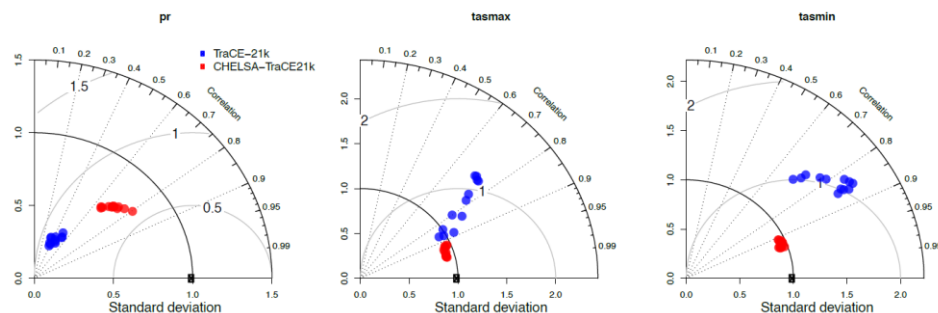


Figure 3: Taylor diagrams comparing the relationship between TraCE-21k (blue) and CHELSA-TraCE21k (red). Data is shown for the 20th century time period with average monthly observational data from the Global Historical Climate Network (GHCN) for the time period 1950-1990. Each dot represents a specific month.

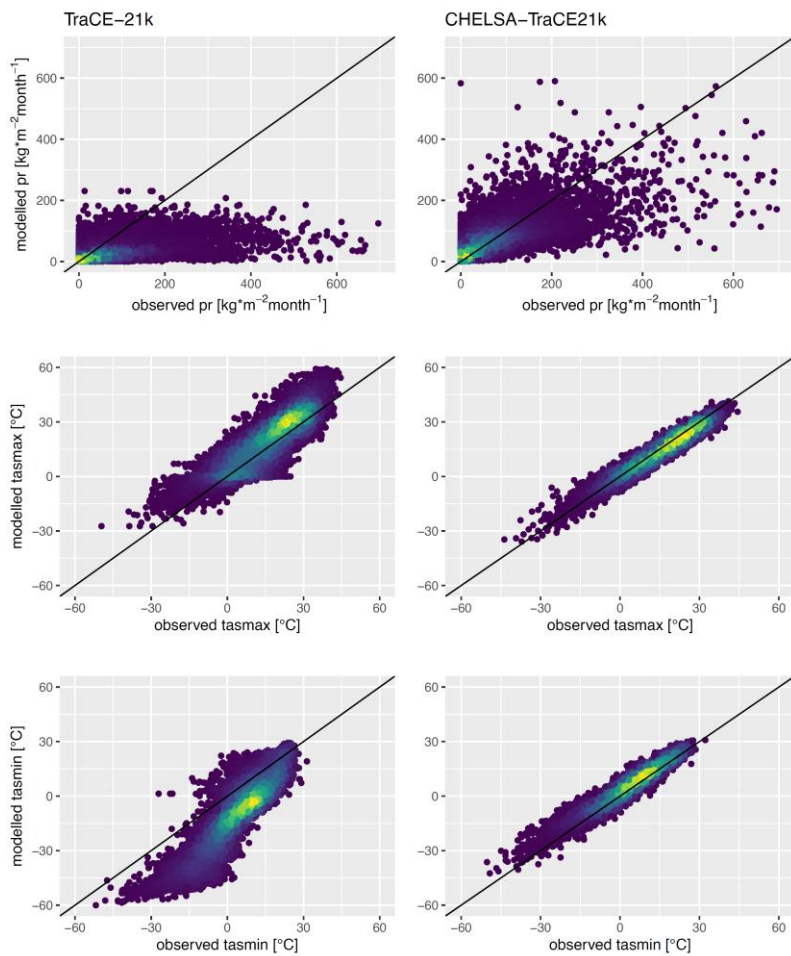


Figure 4: Scatter plots comparing precipitation, maximum-, and minimum temperature. Data are aggregated from TraCE-21k and CHELSA-TraCE21k for the 20th century time period with observational data from the Global Historical Climate Network (GHCN) for the time period 1950-1990.

4.2 Comparison with temperature proxies from ice core data

We compared the downscaled temperatures with the Greenland ice core reconstructions of Buizert et al. (Buizert et al., 2014, 2018) to check the performance of the downscaling at eight ice core locations on the Greenland Ice Sheet (GIS). Although both temperature reconstructions and GCM generated temperatures have uncertainties connected to them (Erb et al., 2018), the ice core data are so far the best possible validation dataset that spans the entire deglaciation period from 21k BP to 1990 (Buizert et al., 2014, 2018). To assess the performance gain of the downscaling over the coarse resolution TraCE21k data, we compare the ice core annual mean near surface temperature reconstructions with both the CHELSA-TraCE21k, and the original TraCE-21k temperature data.

Compared to the temperature reconstructions from ice cores, the downscaled CHELSA-TraCE21k model had reduced bias at four of the ice core sites located at the edges of the GIS (ReCAP, Agassiz, Hans Tausen Iskappe, Camp Century), but increased the bias, RMSE and MAE at the remaining four sites at the center of the GIS (NEEM, NGRIP, GISP2, Dye 3) (Fig. 5). Overall, both CHELSA-TraCE21k as well as TraCE21k show a warm bias before the Heinrich 1 event (i.e. the break off of large groups of icebergs from Greenland into the North Atlantic, 16.8k BP), and roughly after the 8.2k event at four of the sites (ReCAP, Agassiz, Hans Tausen Iskappe, Camp Century). At three sites (ReCAP, Agassiz, Hans Tausen Iskappe, Camp Century) a cold bias is present after the younger Dryas (Fig. 5). At the four other sites, CHELSA-TraCE21k usually shows a warm bias before the H1, and TraCE-21k a cold bias before the H1 (Fig. 5). After the younger dryas (12.9k BP – 11.6k BP), both models show a cold bias at these sites. At the Camp Century site, the Trace data are close to the $\delta^{15}\text{N}$ -based temperature reconstructions before the H1 event, and CHELSA-TraCE21k shows a warm bias, while after the younger dryas the situation is reversed (Fig. 5).

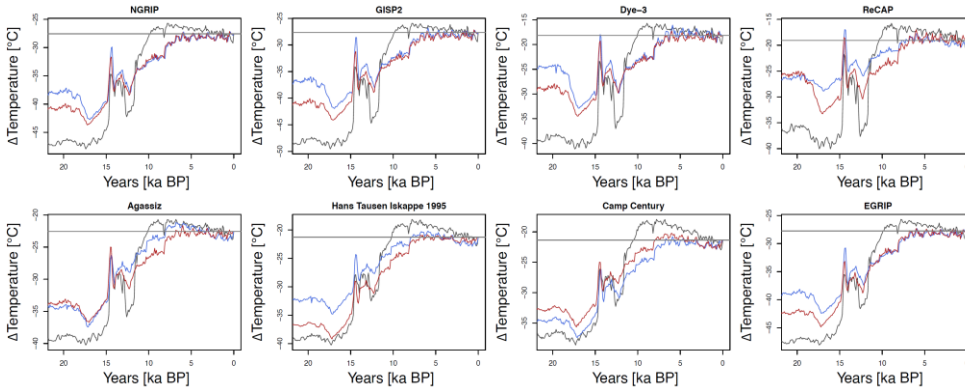


Figure 5: Comparison of temperature anomalies from current (1950-1990) for the CHELSA-TraCE21k time series data (blue), the TraCE21k data (red), and the temperature reconstructions from ice cores (black) for 8 sites across Greenland. The grey horizontal

line indicates the current observed temperature during the period 1981-2010 from CHELSA V2.1. [data](#). Temperatures are plotted as anomalies from the current temperature recorded at the respective location of the ice cores.

The bias observed after downscaling might be related to factors to a bias in all the different input sources, such as the TraCE-21k bias being amplified, a bias in the ice-core proxy data itself, or the bias correction using the relatively simple change factor method. With the available data, these potential causes cannot clearly be disentangled, but should be kept in mind for applications of the data.

4.3 Validation of glacier extent between 18k BP and 1k BP

Although the downscaling algorithm might increase the performance of the temperature and precipitation estimates during the historical period, this does not imply that this improvement is equal during the entire transient time series. To further validate the data, we therefore compared it to more derived parameters for which time series data exists.

As the ice core temperature reconstructions have associated uncertainties, it is impossible to disentangle if potential differences between the ice core data and the model data are due to uncertainties in the reconstructions. To validate the downscaled temperature data further, we used the interpolated extent of glaciers in CHELSA-TraCE21k, and compared it to glacial extent data from Dyke et al. 2003. The data consists of expert delineated glacier maps based on a chronological database of radiocarbon dates and contains > 4000 dates located in North America (Dyke et al., 2003). To compare both datasets, we first calculated the glacial extent from CHELSA-TraCE21k by assigning each 1km grid cell in a Lambert Conformal Conic projection so that each data point compared equals 1 km² either being covered by a glacier [1] or being free of glacier [0]. We assigned a 1 if the simulated glacier height was above the paleo terrain elevation, and a 0 if it was lower or equal to the paleo terrain elevation. The paleo terrain elevation was calculated using the current terrain elevation minus the sea level difference between current and that of the respective paleo timestep. As the current terrain elevation already includes extent glaciers, this elevation dependent procedure of assigning glacial extents would result in the current glaciers being assigned a 0. Therefore, we assigned all grid cells covered by extent glaciers a 1.

To compare the simulated glacial extent to the expert delineated extent, we rasterized the polygons provided by Dyke et al., 2003 for the years 18k BP - 1k BP to the 1km resolution, extent, and projection of the simulated glacial cover and assign a 1 where the polygon intersects with a 1km raster cell and a 0 otherwise.

We then calculated three different test values to identify if the simulations correctly predict the presence and absence of a glacier. As the dataset is highly unbalanced between absences of glaciers [0] and presences of glaciers [1] through time we use balanced accuracy which is defined as: $(sensitivity + specificity)/2$. Additionally we report Cohen's Kappa, and the True Skill Statistic (Allouche et al., 2006).

The test validations of the glacial extent show a good performance over most time steps (Fig. 6), but with a notable drop in accuracy at 8k BP where all validation metrics drop significantly. Aside from the drop at 8k BP, the performance of the glacial

extent simulations performed well. The marked drop in performance around 8k BP might be due to the 8.2k event, which
 marked a strong decrease in global temperatures, most likely due to meltwater fluxes from the collapsing Laurentide ice sheet .
 The strong coupling between temperature and glacial extent in CHELSA-TraCE21k generates an increase in glacial extent
 more than a sudden collapse during this time period, which seems to override the signal from the ICE6G forcing data in
 CHELSA-TraCE21k.

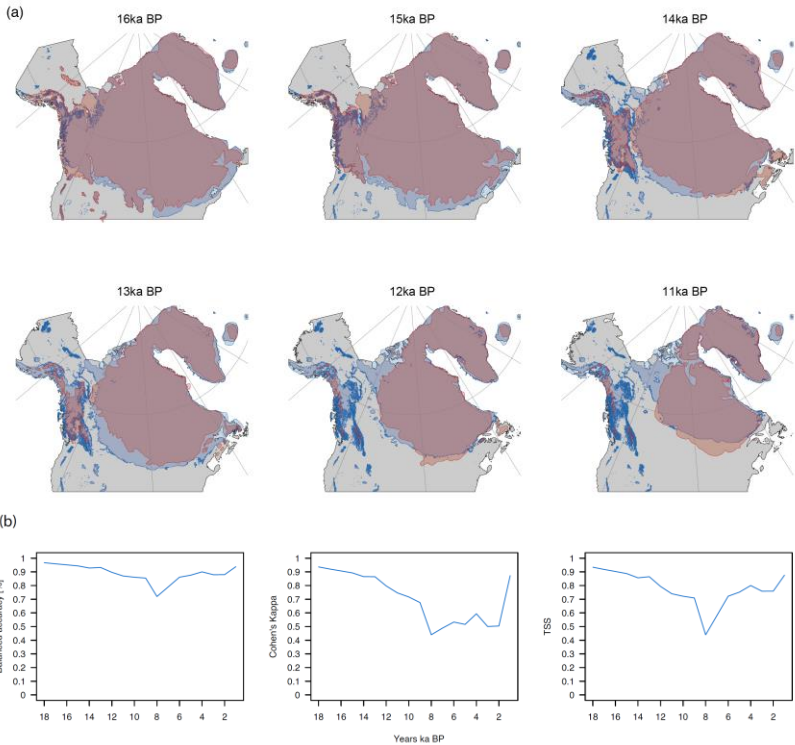


Figure 6: [a.\)](#) Comparisons of estimated glacial extents of the Laurentide ice sheet from 16k BP to 11k BP. Blue delineates the
 interpolated ice sheet extent from CHELSA-TraCE21k, and red shows the estimated extent from (Dyke et al., 2003). While the retreat of the
 main Laurentide ice sheet is similar in both estimations, the Cordilleran Ice sheet covering the Rocky Mountains, retreats faster in
 the estimations by (Dyke et al., 2003), compared to CHELSA-TraCE21. b.) Performance comparison using three different metrics (Balanced
 accuracy, Cohen's Kappa, and True Skill Statistic) from a comparison of CHELSA-TraCE21k and Dyke et al. 2003.

6 Plausibility test using dynamic simulation of effective plant refugia

470 Transient long-term climatic data have a wide range of possible applications, ranging from population genetics (Leugger et al., 2022; Yannic et al., 2020), community ecology (Staples et al., 2022), to evolutionary biology (Cerezzer et al., 2022), just to name a few. Here we use one application in paleo-ecology as plausibility test to additionally check if the transient CHELSA-TraCE21k data is able to reliably detect known LGM refugia of plant species. Climatic changes during the last glacial cycle since the LGM, have had a significant influence on the distribution of ecosystems (Williams and Jackson, 2007), species (Hewitt, 1999; Hampe and Jump, 2011), and as a result on intraspecific genetic structures and speciation (Alsos et al., 2012; Yannic et al., 2014, 2020; Pellissier et al., 2015).

480 Tracing the distribution of species through time is, however, challenging as the spatio-temporal distributions of species strongly depend on environmental suitability (Guisan and Zimmermann, 2000), spatial accessibility of a given location (Svenning and Skov, 2004; Normand et al., 2011), and species dispersal abilities (Engler and Guisan, 2009). A dynamic simulation of species distributions can integrate all these aspects and therefore provides a valuable testbed for climatic data (Nobis and Normand, 2014). However, the spatio-temporal resolution of climate data needed for such simulations have been limited to comparable coarse grain climatic data (Gherghel and Martin, 2020), which usually creates a mismatch between the climate derived from the model and the climate actually experienced by an organism (Seo et al., 2009).

485 Here, we use the downscaled transient temperature and precipitation from CHELSA-TraCE21 since 17k BP (the coldest recorded temperatures in the CHELSA-TraCE21k model for Europe) to reconstruct refugia of the deciduous tree Grey Alder (*Alnus incana*) in Europe before post glacial climate warming. Similar to Nobis & Normand (2014), we first calibrated a generalized linear model (GLM) (Nelder and Wedderburn, 1972) using current presences and absences of Grey Alder within polygons of the *Atlas Florae Europaeae* (AFE) (Kurtto et al., 2018) as the response variable and current annual mean temperature and precipitation from CHELSA-TraCE21k as predictors calculated as zonal mean values of 5 x 5 km rasterized AFE polygons. Despite the simplicity of the model it showed a fair to good model fit with a 10-fold cross-validated AUC value of 0.89.

490 Then, the GLM model was used to predict the suitability of Grey Alder from 17k BP till today in 500-year steps with 5 km resolution and Lambert azimuthal equal-area projection. Glaciated areas were defined as unsuitable and were taken from the CHELSA-TraCE21k glacial reconstructions. We used the resulting time series of climatic suitability as input to the KISSMig (Keep it simple stupid migration) model (Nobis & Normand 2014), which iteratively uses a simple 3 x 3 cell algorithm to calculate the spatial spread from a given origin from 17k BP to present. Presences and absences were weighted equally for the initial GLM calibration and KISSMig used squared suitability values to fulfil basic empirical expectations (see <http://purl.oclc.org/wsl/kissmig>).

495 We tested for each AFE polygon of the current Grey Alder distribution all 25 x 25 km areas across Europe as potential refugia. All 5 x 5 km grid cells of those areas suitable at 17k BP were kept as refugia, if the respective AFE polygon was accessible and the spread pattern generated the lowest number of false positives when compared to the current AFE distribution. Because

500

Field Code Changed

Field Code Changed

Field Code Changed

Formatted: English (United States)

the migration ability of Grey Alder was unknown a priori, KISSMig simulations used one to 10 iterations for each 500-year step, corresponding to a maximum migration rate of 10 to 100 m/a. For each iteration number, the combined spread pattern from all detected effective refugia was compared with the current distribution based on F1-scores. The optimized iteration number was identified by optimizing F1, which showed for Grey Alder a maximum migration rate of 50 m/a. For a comparison with genetic clusters (Dering et al., 2016), the locations of that study were linked to the detected effective refugia with the shortest euclidean distance for simplicity.

Current genetic clustering of populations indicates that the modelling of *A. incana* distributions at 17k BP shows that simulations based on CHELSA-TraCE21k successfully detected glacial refugia in the Southern Alps, southern Norway, northern Norway, the Balkans, and eastern Romania (Fig. 7). The situation in eastern Europe is more complex, with most refugia located in Russia. However, since we only used the current distribution of *A. incana* in western Europe the results might be biased towards the east.

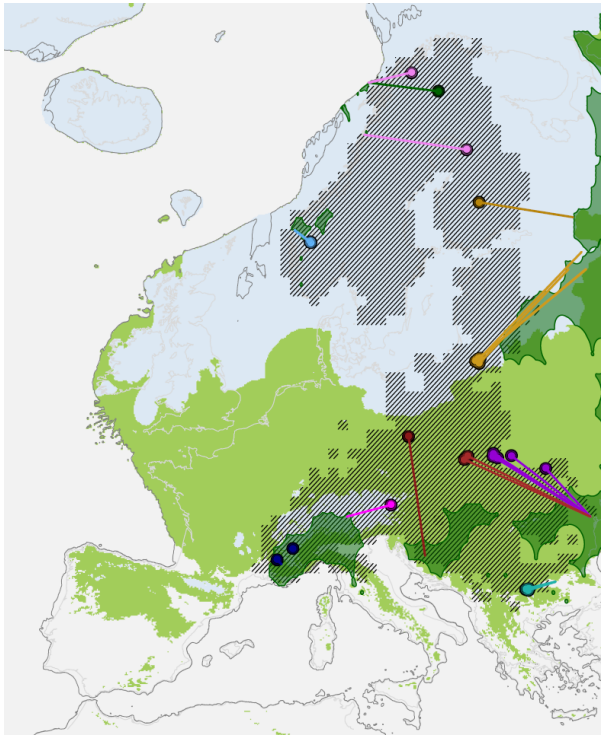


Figure 7: Distribution of *Alnus incana* in Europe (based on the Atlas Flora Europaea (Kurtto et al., 2018)) at current time (line shaded/hatched), and reconstructed effective refugia at 17k BP (dark green alpha hull polygons) using dynamic species distribution modelling based on KISSMig and CHELSA-TraCE21k. The entire suitable habitat for *A. incana* at 17k BP is indicated as light green. Although almost the entire southern-central Europe was suitable for *A. incana* at 17k BP, it might not have occurred at all locations due to dispersal constraints, which are considered in the dark green KISSMig reconstructed distribution. Colored circles indicate the population genetic structure of *A. incana*, taken from Dering et al. 2016, where each color represents a genetic cluster. Lines indicate the most likely effective refugia a genetic cluster can be associated to, given dispersal and climatic constraints. Current genetic clustering of populations indicates that the modelling of *A. incana* distributions at 17k BP successfully detected glacial effective refugia in the Southern Alps (dark blue), southern Norway (light blue), northern Norway (pink), the Balkans (dark red), and eastern Romania (turquoise), and the black sea (dark red and violet). As we only use the current distribution of *A. incana* within the AFE extent the results might be biased outside of it.

7 Conclusions

Although both, the original TraCE-21k, as well as the downscaled CHELSA-Trace21k data track the relative temperature change well compared to ice cores, both models have relatively high temperature biases in absolute temperatures. Both the original data and the downscaled data have a warm bias before the younger Dryas, and a cold bias after it relative to the ice core proxy data. There are several reasons for this: coupled atmosphere ocean general circulation models (GCMs) such as CCSM3 cannot provide regional-scale or unbiased information on a variety of climatic processes (Meehl et al., 2007). Temperatures from ice cores themselves are only based on proxy data, and the overall performance of such proxy data in estimating absolute temperatures is connected to biases in itself (Erb et al., 2018). The downscaling of the CHELSA-Trace21k data involves a trend-preserving (Hempel et al., 2013) change factor step to explicitly preserve the trends in TraCE-21k. If, however, these trends are already underestimated by the TraCE-21k data, they will also be present in the downscaled data. The estimation of glacial extents shows an accuracy of >80% compared to expert delineations of the glacial extent of the Laurentide ice sheet. There is, however, a clear drop in accuracy at the 8k BP event when atmospheric methane concentration decreased leading to a cooling and drying of the northern hemisphere (Kobashi et al., 2007). The strong coupling of the ice interpolations with only temperature might cause the decrease in performance as the downscaling algorithm ignores changes in precipitation that are only present in the driving ICE6G data. As the downscaling assumes an increase in glacial boundaries with cooling, this effect might not be realistic under an overall drying climate, and the fast shifts in temperatures over only 150 years (Kobashi et al., 2007) might also not be well represented in a model with 100 year resolution. Another problem in the estimation of the glacial extent might contain errors from the applied B-spline interpolation. The resulting ice cover from this interpolation can, in some areas, only be a few meters thick, not representing real glaciers, but rather spatial autocorrelation artefact of the interpolation approach used.

The CHELSA-Trace21k data seems to be able to recreate the distribution of temperature and precipitation in a meaningful manner, so that the use of the data in subsequent analysis produces meaningful results. The reconstruction of the refugia for *Alnus incana* shows that the combination of high-resolution climate data, together with a dynamic distribution model was able to accurately detect refugia, even those of a few kilometer in extent (Parducci et al., 2012) that cannot be detected using coarse climate data.

Code availability

Downscaling codes are based on (Karger et al., 2017a), and all modules used are open source and integrated into SAGA-GIS, available here: <https://sourceforge.net/projects/saga-gis/>. The code unique to this study is written in R and creates the paleo-orography and glacier interpolations, and is also available on zenodo (DOI:10.5281/zenodo.4545753).

Data availability

All post-processed data (Karger et al., 2021a) and additional input files other than those provided by TraCE21k can be accessed at the envidat.ch (DOI:10.16904/envidat.211.). The data is published under a Creative Commons Attribution 2.0 Generic (CC BY 2.0) license.

Author contribution

D.N.K., M.N., and N.Z. developed the idea. D.N.K. developed the model and implemented the code. D.N.K. M.N. and S.N. validated the data. N.Z., S.N., and C.H.G. funded the project. D.N.K. wrote the first version of the manuscript and all authors contributed to subsequent revisions.

Competing interest

The authors declare that they have no conflict of interest.

Acknowledgements

D.N.K. & N.E.Z. acknowledge funding from: The WSL internal grants exCHELSA and ClimEx, the Joint Biodiversa COFUND Call on “Biodiversity and Climate Change” (project ‘FeedBaCks’) with the national funder Swiss National Foundation (20BD21_193907), as well as the Swiss Data Science Projects: SPEEDMIND, and COMECO. D.N.K. & C.H.G. acknowledges funding to the ERA-Net BiodivERsA - Belmont Forum, with the national funder Swiss National Foundation (20BD21_184131), part of the 2018 Joint call BiodivERsA-Belmont Forum call (project ‘FutureWeb’), the WSL internal grant ClimEx. S.N. acknowledge funding from Aarhus University Research Foundation.

References

Adams, J. M. and Faure, H.: Preliminary Vegetation Maps of the World since the Last Glacial Maximum: An Aid to Archaeological Understanding, *J. Archaeol. Sci.*, 24, 623–647, <https://doi.org/10.1006/jasc.1996.0146>, 1997.

Allouche, O., Tsoar, A., and Kadmon, R.: Assessing the accuracy of species distribution models: prevalence, kappa and the true skill statistic (TSS), *J. Appl. Ecol.*, 43, 1223–1232, <https://doi.org/10.1111/j.1365-2664.2006.01214.x>, 2006.

- Alsos, I. G., Ehrich, D., Thuiller, W., Eidesen, P. B., Tribsch, A., Schönewetter, P., Lagaye, C., Taberlet, P., and Brochmann, C.: Genetic consequences of climate change for northern plants, *Proc. R. Soc. B Biol. Sci.*, 279, 2042–2051, <https://doi.org/10.1098/rspb.2011.2363>, 2012.
- Argus, D. F., Peltier, W. R., Drummond, R., and Moore, A. W.: The Antarctica component of postglacial rebound model ICE-6G_C (VM5a) based on GPS positioning, exposure age dating of ice thicknesses, and relative sea level histories, *Geophys. J. Int.*, 198, 537–563, <https://doi.org/10.1093/gji/ggu140>, 2014.
- Basist, A., Bell, G. D., and Meentemeyer, V.: Statistical Relationships between Topography and Precipitation Patterns, *J. Clim.*, 7, 1305–1315, [https://doi.org/10.1175/1520-0442\(1994\)007<1305:SRBTAP>2.0.CO;2](https://doi.org/10.1175/1520-0442(1994)007<1305:SRBTAP>2.0.CO;2), 1994.
- Berrisford, P., Dee, D., Fielding, K., Fuentes, M., Kallberg, P., Kobayashi, S., and Uppala, S.: The ERA-interim archive, *ERA Rep. Ser.*, 1–16, 2009.
- Binney, H., Edwards, M., Macias-Fauria, M., Lozhkin, A., Anderson, P., Kaplan, J. O., Andreev, A., Bezrukova, E., Blyakharchuk, T., Jankovska, V., Khazina, I., Krivonogov, S., Kremenetski, K., Nield, J., Novenko, E., Ryabogina, N., Solovieva, N., Willis, K., and Zernitskaya, V.: Vegetation of Eurasia from the last glacial maximum to present: Key biogeographic patterns, *Quat. Sci. Rev.*, 157, 80–97, <https://doi.org/10.1016/j.quascirev.2016.11.022>, 2017.
- Böhner, J.: General climatic controls and topoclimatic variations in Central and High Asia, *Boreas*, 35, 279–295, <https://doi.org/10.1111/j.1502-3885.2006.tb01158.x>, 2006.
- Böhner, J. and Antonic, O.: Böhner, J., & Antonic, O. (2009). Land-Surface Parameters Specific to Topo-Climatology. In T. Hengl, & H. I. Reuter (Eds.), *GEOMORPHOMETRY: CONCEPTS, SOFTWARE, APPLICATIONS* (pp. 195–226). Elsevier Science., in: in T. Hengl, & H. I. Reuter (eds.) *Geomorphometry: Concepts, Software, Applications*, Elsevier Science, 195–226, 2009.
- Brown, J. L., Hill, D. J., Dolan, A. M., Carnaval, A. C., and Haywood, A. M.: PaleoClim, high spatial resolution paleoclimate surfaces for global land areas, *Sci. Data*, 5, 1–9, <https://doi.org/10.1038/sdata.2018.254>, 2018.
- Buizert, C., Gkinis, V., Severinghaus, J. P., He, F., Lecavalier, B. S., Kindler, P., Leuenberger, M., Carlson, A. E., Vinther, B., Masson-Delmotte, V., White, J. W. C., Liu, Z., Otto-Bliesner, B., and Brook, E. J.: Greenland temperature response to climate forcing during the last deglaciation, *Science*, 345, 1177–1180, <https://doi.org/10.1126/science.1254961>, 2014.
- Buizert, C., Keisling, B. A., Box, J. E., He, F., Carlson, A. E., Sinclair, G., and DeConto, R. M.: Greenland-Wide Seasonal Temperatures During the Last Deglaciation, *Geophys. Res. Lett.*, 45, 1905–1914, <https://doi.org/10.1002/2017GL075601>, 2018.
- Carlson, A. E., Ullman, D. J., Anslow, F. S., He, F., Clark, P. U., Liu, Z., and Otto-Bliesner, B. L.: Modeling the surface mass-balance response of the Laurentide Ice Sheet to Bølling warming and its contribution to Meltwater Pulse 1A, *Earth Planet. Sci. Lett.*, 315–316, 24–29, <https://doi.org/10.1016/j.epsl.2011.07.008>, 2012.
- Cerezer, F. O., Machac, A., Rangel, T. F., and Dambros, C. S.: Exceptions to the rule: Relative roles of time, diversification rates and regional energy in shaping the inverse latitudinal diversity gradient, *Glob. Ecol. Biogeogr.*, n/a, <https://doi.org/10.1111/geb.13559>, 2022.
- Daly, C., Taylor, G. H., and Gibson, W. P.: The PRISM approach to mapping precipitation and temperature, *Proc 10th AMS Conf Appl. Climatol.*, 20–23, 1997.

- 610 Danielson, J. J. and Gesch, D. B.: Global multi-resolution terrain elevation data 2010 (GMTED2010), US Geological Survey, 2011.
- Dyke, A. S., Moore, A., and Robertson, L.: Deglaciation of North America, 2003.
- Ehlers, J., Gibbard, P. L., and Hughes, P. D.: Quaternary Glaciations - Extent and Chronology, Volume 15 - 1st Edition, 2011.
- 615 Engler, R. and Guisan, A.: MigClim: Predicting plant distribution and dispersal in a changing climate, *Divers. Distrib.*, 15, 590–601, <https://doi.org/10.1111/j.1472-4642.2009.00566.x>, 2009.
- Erb, M. P., Jackson, C. S., Broccoli, A. J., Lea, D. W., Valdes, P. J., Crucifix, M., and DiNezio, P. N.: Model evidence for a seasonal bias in Antarctic ice cores, *Nat. Commun.*, 9, 1361, <https://doi.org/10.1038/s41467-018-03800-0>, 2018.
- Frei, C. and Schär, C.: A precipitation climatology of the Alps from high-resolution rain-gauge observations, *Int. J. Climatol.*, 18, 873–900, [https://doi.org/10.1002/\(SICI\)1097-0088\(19980630\)18:8<873::AID-JOC255>3.0.CO;2-9](https://doi.org/10.1002/(SICI)1097-0088(19980630)18:8<873::AID-JOC255>3.0.CO;2-9), 1998.
- 620 Frieler, K., Lange, S., Piontek, F., Reyer, C. P. O., Schewe, J., Warszawski, L., Zhao, F., Chini, L., Denvil, S., Emanuel, K., Geiger, T., Halladay, K., Hurtt, G., Mengel, M., Murakami, D., Ostberg, S., Popp, A., Riva, R., Stevanovic, M., Suzuki, T., Volkholz, J., Burke, E., Ciais, P., Ebi, K., Eddy, T. D., Elliott, J., Galbraith, E., Gosling, S. N., Hattermann, F., Hickler, T., Hinkel, J., Hof, C., Huber, V., Jägermeyr, J., Krysanova, V., Marcé, R., Müller Schmied, H., Mouratiadou, I., Pierson, D., Tittensor, D. P., Vautard, R., Vliet, M. van, Biber, M. F., Betts, R. A., Bodirsky, B. L., Deryng, D., Frolking, S., Jones, C. D., Lotze, H. K., Lotze-Campen, H., Sahajpal, R., Thonicke, K., Tian, H., and Yamagata, Y.: Assessing the impacts of 1.5 °C global warming – simulation protocol of the Inter-Sectoral Impact Model Intercomparison Project (ISIMIP2b), *Geosci. Model Dev.*, 10, 4321–4345, <https://doi.org/10.5194/gmd-10-4321-2017>, 2017.
- Fuhrer, O., Chadha, T., Hoefler, T., Kwasniewski, G., Lapillonne, X., Leutwyler, D., Lüthi, D., Osuna, C., Schär, C., 630 Schulthess, T. C., and Vogt, H.: Near-global climate simulation at 1km resolution: establishing a performance baseline on 4888 GPUs with COSMO 5.0, *Geosci. Model Dev.*, 11, 1665–1681, <https://doi.org/10.5194/gmd-11-1665-2018>, 2018.
- Gao, X., Xu, Y., Zhao, Z., Pal, J. S., and Giorgi, F.: On the role of resolution and topography in the simulation of East Asia precipitation, *Theor. Appl. Climatol.*, 86, 173–185, <https://doi.org/10.1007/s00704-005-0214-4>, 2006.
- Gherghel, I. and Martin, R. A.: Postglacial recolonization of North America by spadefoot toads: integrating niche and 635 corridor modeling to study species' range dynamics over geologic time, *Ecography*, 43, 1499–1509, <https://doi.org/10.1111/ecog.04942>, 2020.
- Guisan, A. and Thuiller, W.: Predicting species distribution: offering more than simple habitat models, *Ecol. Lett.*, 8, 993–1009, 2005.
- Guisan, A. and Zimmermann, N. E.: Predictive habitat distribution models in ecology, *Ecol. Model.*, 135, 147–186, 2000.
- 640 Hampe, A. and Jump, A. S.: Climate Relicts: Past, Present, Future, *Annu. Rev. Ecol. Evol. Syst.*, 42, 313–333, <https://doi.org/10.1146/annurev-ecolsys-102710-145015>, 2011.
- Harris, I., Osborn, T. J., Jones, P., and Lister, D.: Version 4 of the CRU TS monthly high-resolution gridded multivariate climate dataset, *Sci. Data*, 7, 1–18, <https://doi.org/10.1038/s41597-020-0453-3>, 2020.
- He, F.: Simulating Transient Climate Evolution of the Last Deglaciation with CCSM3, PhD - Thesis, University of 645 Wisconsin Madison, Madison, WC, USA, 171 pp., 2011.

Hempel, S., Frieler, K., Warszawski, L., Schewe, J., and Piontek, F.: A trend-preserving bias correction—the ISI-MIP approach, *Earth Syst. Dyn.*, 4, 219–236, 2013.

Hewitt, G. M.: Post-glacial re-colonization of European biota, *Biol. J. Linn. Soc.*, 68, 87–112, <https://doi.org/10.1111/j.1095-8312.1999.tb01160.x>, 1999.

650 Hijmans, R. J., Cameron, S. E., Parra, J. L., Jones, P. G., and Jarvis, A.: Very high resolution interpolated climate surfaces for global land areas, *Int. J. Climatol.*, 25, 1965–1978, <https://doi.org/10.1002/joc.1276>, 2005.

Hunter, R. D. and Meentemeyer, R. K.: Climatologically Aided Mapping of Daily Precipitation and Temperature, *J. Appl. Meteorol.*, 44, 1501–1510, <https://doi.org/10.1175/JAM2295.1>, 2005.

655 Hutchinson, G. E.: POPULATION STUDIES - ANIMAL ECOLOGY AND DEMOGRAPHY - CONCLUDING REMARKS, *Cold Spring Harb. Symp. Quant. Biol.*, 22, 415–427, 1957.

Karger, D. N., Conrad, O., Böhner, J., Kawohl, T., Kreft, H., Soria-Auza, R. W., Zimmermann, N. E., Linder, H. P., and Kessler, M.: Climatologies at high resolution for the earth’s land surface areas, *Sci. Data*, 4, 170122, 2017a.

660 Karger, D. N., Conrad, O., Böhner, J., Kawohl, T., Kreft, H., Soria-Auza, R. W., Zimmermann, N. E., Linder, H. P., and Kessler, M.: Climatologies at high resolution for the earth’s land surface areas, *Dryad Digital Repository*, <https://doi.org/10.5061/dryad.kd1d4>, 2017b.

Karger, D. N., Schmatz, D. R., Dettling, G., and Zimmermann, N. E.: High resolution monthly precipitation and temperature timeseries for the period 2006-2100, *Sci. Data*, 2020.

665 Karger, D. N., Nobis, M., Normand, S., Graham, C. H., and Zimmermann, N. E.: CHELSA-TraCE21k: Downscaled transient temperature and precipitation data since the last glacial maximum - *EnviDat*, *enviDat*, <https://doi.org/10.16904/enviDat.211>, 2021a.

Karger, D. N., Wilson, A. M., Mahony, C., Zimmermann, N. E., and Jetz, W.: Global daily 1 km land surface precipitation based on cloud cover-informed downscaling, *Sci. Data*, 8, 307, <https://doi.org/10.1038/s41597-021-01084-6>, 2021b.

670 Kobashi, T., Severinghaus, J. P., Brook, E. J., Barnola, J.-M., and Grachev, A. M.: Precise timing and characterization of abrupt climate change 8200 years ago from air trapped in polar ice, *Quat. Sci. Rev.*, 26, 1212–1222, <https://doi.org/10.1016/j.quascirev.2007.01.009>, 2007.

Körner, C.: The use of ‘altitude’ in ecological research, *Trends Ecol. Evol.*, 22, 569–574, <https://doi.org/10.1016/j.tree.2007.09.006>, 2007.

Kurtto, A., Sennikov, A. B., and Lampinen, R.: *Atlas Florae Europaeae - Distribution of vascular plants in Europe*, *Comm. Mapp. Flora Eur. Soc. Biol. Fenn. Vanamo Hels.* 132 Pp, 23, 106–106, 2018.

675 Lawrence, M. G.: The Relationship between Relative Humidity and the Dewpoint Temperature in Moist Air: A Simple Conversion and Applications, *Bull. Am. Meteorol. Soc.*, 86, 225–234, <https://doi.org/10.1175/BAMS-86-2-225>, 2005.

Lawrimore, J. H., Menne, M. J., Gleason, B. E., Williams, C. N., Wuertz, D. B., Vose, R. S., and Rennie, J.: An overview of the Global Historical Climatology Network monthly mean temperature data set, version 3, *J. Geophys. Res.-Atmospheres*, 116, D19121, <https://doi.org/10.1029/2011jd016187>, 2011.

- 680 Leugger, F., Broquet, T., Karger, D. N., Rioux, D., Buzan, E., Corlatti, L., Crestanello, B., Curt-Grand-Gaudin, N., Hauffe, H. C., Rolečková, B., Šprem, N., Tissot, N., Tissot, S., Valterová, R., Yannic, G., and Pellissier, L.: Dispersal and habitat dynamics shape the genetic structure of the Northern chamois in the Alps, *J. Biogeogr.*, n/a, <https://doi.org/10.1111/jbi.14363>, 2022.
- 685 Liu, M., Bárdossy, A., and Zehe, E.: Interaction of valleys and circulation patterns (CPs) on small-scale spatial precipitation distribution in the complex terrain of southern Germany., *Hydrol. Earth Syst. Sci. Discuss.*, 9, 2012.
- Liu, Z., Otto-Bliesner, B. L., He, F., Brady, E. C., Tomas, R., Clark, P. U., Carlson, A. E., Lynch-Stieglitz, J., Curry, W., Brook, E., Erickson, D., Jacob, R., Kutzbach, J., and Cheng, J.: Transient Simulation of Last Deglaciation with a New Mechanism for Bølling-Allerød Warming, *Science*, 325, 310–314, <https://doi.org/10.1126/science.1171041>, 2009.
- 690 Maraun, D.: Bias correction, quantile mapping, and downscaling: Revisiting the inflation issue, *J. Clim.*, 26, 2137–2143, 2013.
- Maraun, D.: Bias Correcting Climate Change Simulations - a Critical Review, *Curr. Clim. Change Rep.*, 2, 211–220, <https://doi.org/10.1007/s40641-016-0050-x>, 2016.
- Maraun, D., Wetterhall, F., Ireson, A. M., Chandler, R. E., Kendon, E. J., Widmann, M., Brienens, S., Rust, H. W., Sauter, T., Themeßl, M., Venema, V. K. C., Chun, K. P., Goodess, C. M., Jones, R. G., Onof, C., Vrac, M., and Thiele-Eich, I.:
695 Precipitation downscaling under climate change: Recent developments to bridge the gap between dynamical models and the end user, *Rev. Geophys.*, 48, RG3003, <https://doi.org/10.1029/2009RG000314>, 2010.
- Marcott, S. A., Clark, P. U., Padman, L., Klinkhammer, G. P., Springer, S. R., Liu, Z., Otto-Bliesner, B. L., Carlson, A. E., Ungerer, A., Padman, J., He, F., Cheng, J., and Schmittner, A.: Ice-shelf collapse from subsurface warming as a trigger for Heinrich events, *Proc. Natl. Acad. Sci.*, 108, 13415–13419, <https://doi.org/10.1073/pnas.1104772108>, 2011.
- 700 McMaster, G. S. and Wilhelm, W.: Growing degree-days: one equation, two interpretations, 1997.
- Meehl, G. A., Stocker, T. F., Collins, W. D., Friedlingstein, P., Gaye, A. T., Gregory, J. M., Kitoh, A., Knutti, R., Murphy, J. M., Noda, A., Raper, S. C. B., Watterson, I. G., Weaver, A. J., and Zhao, Z.-C.: Global climate projections, in: *Climate Change 2007: The Physical Science Basis. Contribution of Working Group I to the Fourth Assessment Report of the Intergovernmental Panel on Climate Change*, Cambridge University Press, Cambridge, UK, 2007.
- 705 Meyer-Christoffer, A., Becker, A., Finger, P., Rudolf, B., Schneider, U., and Ziese, M.: GPCC Climatology Version 2015 at 0.25°: Monthly Land-Surface Precipitation Climatology for Every Month and the Total Year from Rain-Gauges built on GTS-based and Historic Data., *Glob. Precip. Climatol. Cent. GPCC*, https://doi.org/10.5676/DWD_GPCC/CLIM_M_V2015_025, 2015.
- 710 Miller, K. G., Kominz, M. A., Browning, J. V., Wright, J. D., Mountain, G. S., Katz, M. E., Sugarman, P. J., Cramer, B. S., Christie-Blick, N., and Pekar, S. F.: The Phanerozoic Record of Global Sea-Level Change, *Science*, 310, 1293–1298, <https://doi.org/10.1126/science.1116412>, 2005.
- Nelder, J. A. and Wedderburn, R. W. M.: Generalized Linear Models, *J. R. Stat. Soc. Ser. Gen.*, 135, 370–384, <https://doi.org/10.2307/2344614>, 1972.
- Neumann, P., Düben, P., Adamidis, P., Bauer, P., Brück, M., Kornblueh, L., Klocke, D., Stevens, B., Wedi, N., and Biercamp, J.: Assessing the scales in numerical weather and climate predictions: will exascale be the rescue?, *Philos. Trans. R. Soc. Math. Phys. Eng. Sci.*, 377, 20180148, <https://doi.org/10.1098/rsta.2018.0148>, 2019.

Formatted: Font: (Default) Times New Roman, 10 pt, French (Switzerland)

- Nobis, M. P. and Normand, S.: KISSMig – a simple model for R to account for limited migration in analyses of species distributions, *Ecography*, 37, 1282–1287, <https://doi.org/10.1111/ecog.00930>, 2014.
- 720 Normand, S., Ricklefs, R. E., Skov, F., Bladt, J., Tackenberg, O., and Svenning, J.-C.: Postglacial migration supplements climate in determining plant species ranges in Europe, *Proc. R. Soc. Lond. B Biol. Sci.*, rspb20102769, <https://doi.org/10.1098/rspb.2010.2769>, 2011.
- Oke, T. R.: *Boundary layer climates*, Routledge, 464 pp., 2002.
- Otto-Bliesner, B. L., Brady, E. C., Clauzet, G., Tomas, R., Levis, S., and Kothavala, Z.: Last Glacial Maximum and Holocene Climate in CCSM3, *J. Clim.*, 19, 2526–2544, <https://doi.org/10.1175/JCLI3748.1>, 2006.
- 725 Pellissier, L., Eidesen, P. B., Ehrich, D., Descombes, P., Schönswetter, P., Tribsch, A., Westergaard, K. B., Alvarez, N., Guisan, A., Zimmermann, N. E., Normand, S., Vittoz, P., Luoto, M., Damgaard, C., Brochmann, C., Wisz, M. S., and Alsos, I. G.: Past climate-driven range shifts and population genetic diversity in arctic plants, *J. Biogeogr.*, n/a-n/a, <https://doi.org/10.1111/jbi.12657>, 2015.
- 730 Peltier, W. R.: Global glacial isostasy and the surface of the ice-age earth: The ICE-5G (CM2) Model and GRACE, *Annu. Rev. Earth Planet. Sci.*, 32, 111–149, <https://doi.org/10.1146/annurev.earth.32.082503.144359>, 2004.
- Peltier, W. R., Argus, D. F., and Drummond, R.: Space geodesy constrains ice age terminal deglaciation: The global ICE-6G_C (VM5a) model, *J. Geophys. Res. Solid Earth*, 120, 450–487, <https://doi.org/10.1002/2014JB011176>, 2015.
- Prentice, I. C., Bartlein, P. J., and Webb, T.: Vegetation and Climate Change in Eastern North America Since the Last Glacial Maximum, *Ecology*, 72, 2038–2056, <https://doi.org/10.2307/1941558>, 1991.
- 735 Raup, B., Racoviteanu, A., Khalsa, S. J. S., Helm, C., Armstrong, R., and Arnaud, Y.: The GLIMS geospatial glacier database: A new tool for studying glacier change, *Glob. Planet. Change*, 56, 101–110, <https://doi.org/10.1016/j.gloplacha.2006.07.018>, 2007.
- Rotunno, R. and Houze, R. A.: Lessons on orographic precipitation from the Mesoscale Alpine Programme, *Q. J. R. Meteorol. Soc.*, 133, 811–830, <https://doi.org/10.1002/qj.67>, 2007.
- 740 Schär, C., Fuhrer, O., Arteaga, A., Ban, N., Charpillot, C., Di Girolamo, S., Hentgen, L., Hoefler, T., Lapillonne, X., Leutwyler, D., Osterried, K., Panosetti, D., Rüdissühli, S., Schlemmer, L., Schulthess, T., Sprenger, M., Ubbiali, S., and Wernli, H.: Kilometer-scale climate models: Prospects and challenges, *Bull. Am. Meteorol. Soc.*, 101, <https://doi.org/10.1175/BAMS-D-18-0167.1>, 2019.
- 745 Schmidli, J., Frei, C., and Vidale, P. L.: Downscaling from GCM precipitation: a benchmark for dynamical and statistical downscaling methods, *Int. J. Climatol.*, 26, 679–689, <https://doi.org/10.1002/joc.1287>, 2006.
- Schulthess, T. C., Bauer, P., Wedi, N., Fuhrer, O., Hoefler, T., and Schär, C.: Reflecting on the goal and baseline for exascale computing: a roadmap based on weather and climate simulations, *Comput. Sci. Eng.*, 21, 30–41, 2018.
- Scotese, C. R.: *Atlas of earth history*, PALEOMAP project, 2001.
- 750 Seo, C., Thorne, J. H., Hannah, L., and Thuiller, W.: Scale effects in species distribution models: implications for conservation planning under climate change, *Biol. Lett.*, 5, 39–43, <https://doi.org/10.1098/rsbl.2008.0476>, 2009.

- Sepulchre, P., Caubel, A., Ladant, J.-B., Bopp, L., Boucher, O., Braconnot, P., Brockmann, P., Cozic, A., Donnadieu, Y., Dufresne, J.-L., Estella-Perez, V., Ethé, C., Fluteau, F., Foujols, M.-A., Gastineau, G., Ghattas, J., Hauglustaine, D., Hourdin, F., Kageyama, M., Khodri, M., Marti, O., Meurdesoif, Y., Mignot, J., Sarr, A.-C., Servonnat, J., Swingedouw, D., Szopa, S., and Tardif, D.: IPSL-CM5A2 – an Earth system model designed for multi-millennial climate simulations, *Geosci. Model Dev.*, 13, 3011–3053, <https://doi.org/10.5194/gmd-13-3011-2020>, 2020.
- 755 Sevruk, B.: Regional Dependency of Precipitation-Altitude Relationship in the Swiss Alps, in: *Climatic Change at High Elevation Sites*, edited by: Diaz, H. F., Beniston, M., and Bradley, R. S., Springer Netherlands, 123–137, https://doi.org/10.1007/978-94-015-8905-5_7, 1997.
- 760 Skamarock, C., Klemp, B., Dudhia, J., Gill, O., Liu, Z., Berner, J., Wang, W., Powers, G., Duda, G., Barker, D., and Huang, X.: A Description of the Advanced Research WRF Model Version 4, OpenSky, <https://doi.org/10.5065/1dfh-6p97>, 2019.
- Soria-Auza, R. W., Kessler, M., Bach, K., Barajas-Barbosa, P. M., Lehnert, M., Herzog, S. K., and Böhner, J.: Impact of the quality of climate models for modelling species occurrences in countries with poor climatic documentation: a case study from Bolivia, *Ecol. Model.*, 221, 1221–1229, 2010.
- 765 Spreen, W. C.: A determination of the effect of topography upon precipitation, *Eos Trans. Am. Geophys. Union*, 28, 285–290, <https://doi.org/10.1029/TR028i002p00285>, 1947.
- Staples, T. L., Kiessling, W., and Pandolfi, J. M.: Emergence patterns of locally novel plant communities driven by past climate change and modern anthropogenic impacts, *Ecol. Lett.*, 25, 1497–1509, <https://doi.org/10.1111/ele.14016>, 2022.
- Stull, R. B.: *An introduction to boundary layer meteorology*, Springer Science & Business Media, 2012.
- 770 Svenning, J.-C. and Skov, F.: Limited filling of the potential range in European tree species, *Ecol. Lett.*, 7, 565–573, <https://doi.org/10.1111/j.1461-0248.2004.00614.x>, 2004.
- Velichko, A. A., Andreev, A. A., and Klimanov, V. A.: Climate and vegetation dynamics in the tundra and forest zone during the late glacial and holocene, *Quat. Int.*, 41–42, 71–96, [https://doi.org/10.1016/S1040-6182\(96\)00039-0](https://doi.org/10.1016/S1040-6182(96)00039-0), 1997.
- 775 Weatherall, P., Marks, K. M., Jakobsson, M., Schmitt, T., Tani, S., Arndt, J. E., Rovere, M., Chayes, D., Ferrini, V., and Wigley, R.: A new digital bathymetric model of the world’s oceans, *Earth Space Sci.*, 2, 331–345, <https://doi.org/10.1002/2015EA000107>, 2015.
- Weischet, W. and Endlicher, W.: *Einführung in die Allgemeine Klimatologie*, Schweizerbart Science Publishers, Stuttgart, Germany, 342 pp., 2008.
- 780 Wilby, R. L., Wigley, T. M. L., Conway, D., Jones, P. D., Hewitson, B. C., Main, J., and Wilks, D. S.: Statistical downscaling of general circulation model output: A comparison of methods, *Water Resour. Res.*, 34, 2995–3008, <https://doi.org/10.1029/98WR02577>, 1998.
- Williams, J. W. and Jackson, S. T.: Novel climates, no-analog communities, and ecological surprises, *Front. Ecol. Environ.*, 5, 475–482, 2007.
- Williams, J. W., Shuman, B. N., III, T. W., Bartlein, P. J., and Leduc, P. L.: Late-Quaternary Vegetation Dynamics in North America: Scaling from Taxa to Biomes, *Ecol. Monogr.*, 74, 309–334, 2004.
- 785 Willmott, C. J. and Robeson, S. M.: Climatologically aided interpolation (CAI) of terrestrial air temperature, *Int. J. Climatol.*, 15, 221–229, <https://doi.org/10.1002/joc.3370150207>, 1995.

Wood, A. W., Leung, L. R., Sridhar, V., and Lettenmaier, D. P.: Hydrologic Implications of Dynamical and Statistical Approaches to Downscaling Climate Model Outputs, *Clim. Change*, 62, 189–216, <https://doi.org/10.1023/B:CLIM.0000013685.99609.9e>, 2004.

790 Woodward, F. I., Fogg, G. E., Heber, U., Laws, R. M., and Franks, F.: The impact of low temperatures in controlling the geographical distribution of plants, *Philos. Trans. R. Soc. Lond. B Biol. Sci.*, 326, 585–593, <https://doi.org/10.1098/rstb.1990.0033>, 1990.

Yannic, G., Pellissier, L., Ortego, J., Lecomte, N., Couturier, S., Cuyler, C., Dussault, C., Hundertmark, K. J., Irvine, R. J., Jenkins, D. A., Kolpashikov, L., Mager, K., Musiani, M., Parker, K. L., Røed, K. H., Sipko, T., Pórisson, S. G., Weckworth, 795 B. V., Guisan, A., Bernatchez, L., and Côté, S. D.: Genetic diversity in caribou linked to past and future climate change, *Nat. Clim. Change*, 4, 132–137, <https://doi.org/10.1038/nclimate2074>, 2014.

Yannic, G., Hagen, O., Leugger, F., Karger, D. N., and Pellissier, L.: Harnessing paleo-environmental modeling and genetic data to predict intraspecific genetic structure, *Evol. Appl.*, 13, 1526–1542, <https://doi.org/10.1111/eva.12986>, 2020.

Yu, Z., Loisel, J., Brosseau, D. P., Beilman, D. W., and Hunt, S. J.: Global peatland dynamics since the Last Glacial 800 Maximum, *Geophys. Res. Lett.*, 37, <https://doi.org/10.1029/2010GL043584>, 2010.